Combust. Sci. and Tech., 178: 193–227, 2006
Copyright © Taylor & Francis LLC
ISSN: 0010-2202 print/1563-521X online
DOI: 10.1080/00102200500287613

Taylor & Francis
Taylor & Francis Group

CRYOGENIC FLUID JETS AND MIXING LAYERS IN TRANSCRITICAL AND SUPERCRITICAL ENVIRONMENTS

NAN ZONG
VIGOR YANG*

Department of Mechanical and Nuclear Engineering, The Pennsylvania State University, University Park, Pennsylvania, USA

This paper provides an overview of recent advances in the theoretical modeling and numerical simulation of cryogenic fluid injection and mixing in transcritical and supercritical environments. The basis of the analysis is a general theoretical and numerical framework that accommodates full conservation laws and real-fluid thermodynamic and transport phenomena. All of the thermophysical properties are determined directly from fundamental thermodynamics theories, along with the use of corresponding-state principles. Turbulence closure is achieved using a large-eddy-simulation technique, in which large-scale motions are calculated explicitly and the effects of unresolved small-scale turbulence are modeled either analytically or empirically. The analysis has been applied to study: (1) fluid jet dynamics, (2) swirl injection of liquid oxygen through a simplex swirl injector, and (3) shear co-axial injection and mixing of liquid oxygen and methane. Various effects, including density stratification, shear-layer instability, volume dilatation, and property variations, dictating the evolution of cryogenic jets and mixing layers, are identified and analyzed in depth. The jet dynamics are found to be largely determined by the local thermodynamic state through its influence on the

Received 5 February, 2005; accepted 26 July, 2005.

This work was sponsored by the Air Force Office of Scientific Research, Grant No. F49620-01-1-0114. The support and encouragement of Dr. Mitat A. Birkan are gratefully acknowledged.

***Address correspondence to vigor@psu.edu**

thermophysical properties of the fluid. The impact of injector configuration and operating conditions on the swirl injector behavior are also highlighted. These results not only shed light on the subject problems, but also provide a quantitative basis for identifying the design parameters and flow variables that exert the strongest influence on the underlying processes.

Keywords: supercritical combustion, liquid propellant rockets, jet phenomena

INTRODUCTION

The demand for performance enhancement and design optimization for high-pressure combustion devices (such as liquid-propellant rockets and gas-turbine and diesel engines) requires a comprehensive understanding of fluid injection and mixing in various transcritical and supercritical environments. In contrast to the wealth of knowledge about these processes at low pressures, information concerning supercritical fluid dynamics appears to be limited. Much of the progress achieved in this field was motivated by the development of advanced cryogenic-propellant rocket engines in the past decade. An assessment of the state of the art up to 2000 was given by Yang (2000). The present work summarizes recent advances in the modeling and simulation of cryogenic fluid jets and mixing layers under conditions representative of contemporary rocket engines. The issue of combustion is addressed in a companion paper by Oefelein (2005) in this special issue.

Extensive efforts have been made to experimentally characterize the dynamics of supercritical fluid injection and mixing (Mayer and Smith, 2004; Oschwald et al., 2005). The studies included injection of liquid nitrogen and coaxial injection of liquid nitrogen and gaseous helium into vessels preconditioned with high-pressure gaseous nitrogen (Branam and Mayer, 2003; Chehroudi et al., 2002a, 2002b; Mayer et al., 2000; Mayer and Smith, 2004; Oschwald and Schik, 1999). Shadowgraph images indicated drastic changes in jet surface phenomena when the chamber pressure reached the critical pressure of the injectant. Ligaments and droplets formed at subcritical pressures, but disappeared at near-critical and supercritical conditions due to the prevalence of turbulent motion and the decrease in surface tension. The jet surface topology bore a strong resemblance to its gaseous counterpart, with the spatial growth rate following that of an incompressible variable-density gaseous jet.

Quantitative information, such as density distribution, was obtained by a spontaneous Raman Scattering technique. The effect of acoustic excitation on the evolution of a cryogenic nitrogen jet was also studied (Chehroudi and Talley, 2002; Davis and Chehroudi, 2004). The influence was substantial at subcritical conditions, but become unnoticeable at supercritical conditions.

In addition to cold-flow experiments, the flame dynamics of shear-coaxial injectors with liquid oxygen (LOX) and hydrogen were systematically investigated, as detailed by Mayer and Smith (2004) and in the papers by Habiballah et al. (2005) and Candel et al. (2005) in this issue. Herding et al. (1998) examined the flame-zone physiochemistry in a pressure range of 5–10 atm using planar laser induced fluorescence of OH radicals and O_2. Kendrick et al. (1999) investigated the effects of LOX post recess on the flame stabilization and spreading processes. Juniper et al. (2000) studied the influence of momentum flux ratio on flame evolution at pressures between 5 and 70 atm. Mayer and colleagues (Ivancic and Mayer, 2002; Mayer and Tamura, 1996; Mayer et al., 2001) conducted a series of experiments over a pressure range of up to 100 atm to identify the flame anchoring mechanism and characterize the injector behavior by means of shadowgraph images. The flame was stabilized by the tiny recirculating flow immediately downstream of the LOX post, with a thickness as small as 0.3 mm. The work on LOX/hydrogen injectors was recently extended to systems involving LOX and hydrocarbon fuels (in particular methane) (Singla et al., 2004; Zurbach et al., 2003) in support of the development of new rocket engines for space transportation.

Compared with shear-coaxial injectors, swirl injectors produce improved intraelement mixing because of the radial momentum imparted to the swirling sheet of liquid propellant. This kind of injectors has been implemented in many operational rocket engines in Russia and the former Soviet Union (Bazarov et al., 2004). Notable examples are the preburner and main-combustor injectors in the RD-170 engine, which have chamber pressures of 530 and 250 atm, respectively. Hulka and colleagues (Hulka and Schneider, 1991, 1993; Hulka and Makel, 1993) conducted a series of cold-flow studies using water and inert gases as propellant simulants to optimize the design of rocket swirl injectors. In a similar experiment using water/nitrogen as injectants, Sasaki et al. (1997) observed self-induced pulsations in swirl coaxial injectors with recessed LOX posts, which may trigger combustion instabilities in rocket

engines. This phenomenon and related injector dynamics can be explained by the theories described by Bazarov and Yang (1998) and Bazarov et al. (2004). Strakey et al. (2001) studied the characteristics of swirl coaxial injectors over a broad range of gas/liquid momentum ratios (1–100) at a chamber pressure of 30 atm using water and helium/nitrogen as propellant simulants. Although the spreading angle of the liquid sheet at a high momentum ratio was less than that reported at one atmosphere, the resultant droplet size is smaller than its counterpart for a shear coaxial injector.

In parallel with experimental studies, substantial progress has been made in the modeling and simulation of supercritical fluid injection and mixing. Oefelein and Yang (1998) performed a pioneering analysis of supercritical mixing and combustion of oxygen and hydrogen. A comprehensive model was established to accommodate real-fluid thermodynamics and transport, with turbulence closure achieved by means of a large-eddy-simulation (LES) technique. The model was recently extended to investigate the three-dimensional flow evolution and flame structure in a shear coaxial uni-element model rocket (Oefelein, 2003). Bellan and colleagues directly simulated the temporal evolution of heptane/nitrogen and oxygen/hydrogen mixing layers under supercritical conditions (Miller et al., 2001; Okong'o et al., 2002; Okong'o and Bellan, 2002, 2004). Zong and Yang systematically preformed LES studies on the dynamics of a single nitrogen fluid jet (Zong et al., 2004; Zong, 2005), swirl injection of oxygen (Zong and Yang, 2004), and shear coaxial injection and mixing of oxygen and methane (Zong and Yang, 2005a) under supercritical conditions.

The present work provides an overview of recent advances in theoretical modeling and numerical simulations of cryogenic fluid injection and mixing under transcritical and supercritical conditions. Emphasis is placed on the detailed flow dynamics and influence of real fluid thermodynamics and transport on flow evolution. The remainder of this paper is organized as follows. Next, we briefly describe the theoretical and numerical framework, including LES formulation and thermophysical property evaluation. A unified thermodynamic treatment for general fluid mixtures over a wide range of flow conditions is also introduced. Major results are presented, covering three subjects: (1) injection of cryogenic fluids; (2) swirl injection of liquid oxygen through simplex injectors; and (3) shear coaxial injection and mixing of liquid oxygen and methane. Finally, a brief summary concludes the work.

THEORETICAL AND NUMERICAL FRAMEWORK

The basis of the analysis is the general theoretical and numerical framework described in Oefelein and Yang (1998), Meng and Yang (2003), Zong et al. (2004), and Meng et al. (2005). The formulation accommodates full conservation laws and real-fluid thermodynamics and transport over the entire temperature and pressure regime of concern. Turbulence closure is achieved by means of a large-eddy-simulation (LES) technique, in which large-scale motions are calculated explicitly and the effects of unresolved small-scale turbulence are modeled either analytically or empirically. The governing Favre-filtered conservation equations are derived by filtering small-scale dynamics from resolved scales over a well-defined set of spatial and temporal intervals. The effects of subgrid-scale (*sgs*) motions are treated using the model proposed by Erlebacher et al. (1992). It employs a Favre-averaged generalization of the Smagorinsky eddy viscosity model coupled with a gradient-diffusion assumption to simulate *sgs* energy and species transport processes. Thermodynamic properties, such as enthalpy, Gibbs energy, and constant-pressure specific heat, are obtained directly from fundamental thermodynamics theories and a modified Soave–Redlich–Kwong (SRK) equation of state (Graboski and Daubert, 1978). Transport properties, such as viscosity and thermal conductivity, are evaluated using an extended corresponding-state theory (Ely and Hanley, 1981, 1983) along with the 32-term Benedict–Webb–Rubin equation of state (Jacobsen and Stewart, 1973). Mass diffusivity is obtained by the Takahashi method, calibrated for high pressure conditions (Takahashi, 1974). The implementation and validation of the property evaluation schemes were detailed in Yang (2000) and Meng et al. (2005).

The theoretical formulation outlined above requires a robust computational scheme, due to the numerical stiffness caused by rapid flow property variations and wide disparities of the characteristic time and length scales involved. A unified treatment of general fluid thermodynamics, based on the concepts of partial-mass and partial-density properties, and valid for the entire fluid states, is established and incorporated into a preconditioning scheme (Meng and Yang, 2003; Zong and Yang, 2005b). Because all of the numerical relations, including the Jacobian matrices and eigenvalues, are derived directly from fundamental thermodynamics theories, the algorithm is self-consistent and capable of solving fluid flows at all speeds and at all fluid thermodynamic states.

The numerical framework employs a density-based, finite volume methodology along with a dual time-step integration technique (Hsieh and Yang, 1997). Temporal discretization is obtained using second-order backward differencing, and the inner-loop pseudo-time term is integrated with a four-step Runge–Kutta scheme. Spatial discretization is achieved with a fourth-order, central-difference scheme in generalized coordinates. Fourth-order scalar dissipation with a total-variation-diminishing switch developed by Swanson and Turkel (1992) is implemented to ensure computational stability and to prevent numerical oscillations in regions with steep gradients. The effect of numerical dissipation on the overall simulation accuracy is analyzed based on the methodology suggested by Wang et al. (2005). It is found that for moderate resolutions within the context of LES, the *sgs* terms are dominant, and artificial dissipation only serves to obtain numerical robustness. A multiblock domain decomposition technique, along with static load balance, is employed to facilitate the implementation of parallel computation with message passing interfaces (MPI) at the domain boundaries.

CRYOGENIC FLUID JET DYNAMICS

As a first step toward the establishment of a comprehensive knowledge base on fluid-mechanic and transport processes in a liquid-propellant rocket combustor, we considered the dynamics of a jet of cryogenic fluid injected at a subcritical temperature into a supercritical environment, in which both the pressure and temperature exceed the thermodynamic critical state of the injectant (Zong et al., 2004, Zong, 2005). Liquid nitrogen with an initial subcritical temperature of 120 K is injected through a circular tube with a diameter of 254 μm into a supercritical nitrogen environment, as shown in Figure 1. A turbulent pipe flow with a bulk velocity of 15 m/s is assumed at the injector exit. The ambient temperature remains at 300 K, but the pressure varies from 69 to 93 atm, comparable to the chamber pressures of many operational rocket engines. For reference, the critical temperature and pressure of nitrogen are 126 K and 34 atm, respectively. The flow conditions summarized in Table 1 simulate the experiments conducted by Chehroudi et al. (2002a). The subscripts ∞ and *inj* denote the ambient and injection conditions, respectively. The Reynolds number is defined as $Re = \rho_{inj} u_{inj} D_{inj} / \mu_{inj}$.

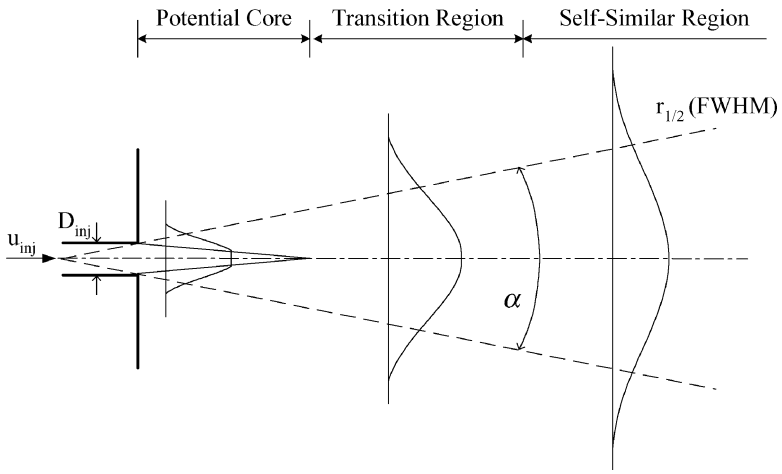

Figure 1. Schematic of fluid jet evolution.

The computational domain extends $40D_{inj}$ axially downstream of the injector exit and $6D_{inj}$ radially from the centerline to minimize the effects of the truncated far-field boundary on the near-field jet evolution (Zong et al., 2004). The entire grid system consists of $225 \times 90 \times 72$ points along the axial, radial, and azimuthal directions, respectively. The grids are clustered in the shear layer and near the injector to resolve rapid property variations in those regions. The mean grid size falls roughly in the inertial subrange of the turbulent kinetic energy spectrum, estimated using the Kolmogorov–Obukhow theory. The smallest grid size is $2\,\mu$m. The computational domain is divided into 54 blocks, with each calculated on a single processor of a distributed-memory parallel computer. The physical time step is 1×10^{-3} ms and the maximum CFL number for the inner-loop pseudo-time integration is 0.7. For each case, the calculation is first conducted for an extended period until the flowfield reaches a stationary state. The time stamp is then reset, and data is

Table 1. Simulation conditions for cryogenic fluid jet dynamics

	p_∞ (MPa)	T_{inj} (K)	T_∞ (K)	ρ_{inj} (kg/m^3)	ρ_∞ (kg/m^3)	u_{inj} (m/s)	ρ_{inj}/ρ_∞	Re
Case 1	6.9	120	300	603	77	15	7.83	44700
Case 2	9.3	120	300	626	103	15	6.07	42300

collected for more than 12 flow-through times (i.e., 15 ms) to obtain statistically meaningful turbulence properties.

Figure 2 shows snapshots of the vorticity-magnitude, density-gradient magnitude, thermal-diffusivity, and compressibility-factor fields for two different ambient pressures, 6.9 and 9.3 MPa. The thermophysical properties are normalized with respect to the values of the injected fluid. The small structures in the vorticity field near the injector arise from the imposed turbulence at the inlet. In both cases, the jet surfaces exhibit tiny instability waves immediately downstream of the injector. These waves then grow and roll up into a succession of ring vortices. The resultant large-scale vortical motion facilitates the mixing of jet with the ambient flow, and causes the entrainment of warmer and irrotational fluid into the jet. In the density-gradient field, a series of finger or thread-like entities emerge from the jet surface and dissolve gradually into the ambience. Similar structures were observed in the experiments by Chehroudi et al. (2002a, 2002b) under the same flow conditions.

Due to the strong initial density stratification between the injected and ambient fluids, a string of large density-gradient regions forms around the jet core. Strong anisotropy of turbulence occurs close to this density interface, where large eddies of integral-length scales become flattened, and the vertical component of the turbulent kinetic energy (TKE) is transferred to its horizontal counterpart (Atsavapranee and Gharib, 1997; Hannoun et al., 1988; Zong et al., 2004). This redistribution of TKE among the spatial constituents makes important changes in the amount of energy available for fluid mixing in the shear layer. The density stratification effectively suppresses radial velocity fluctuations in the flow field and inhibits the development of instability waves. Compared with incompressible turbulent jets, both vortex roll-up and pairing are delayed, leading to a longer potential core around $8D_{inj}$ for the case of $p_\infty = 6.9$ MPa. The length of the potential core for an incompressible turbulent jet is approximately 3–5 times the injector diameter (Ho and Huerre, 1984). The influence of density stratification decreases with increasing pressure. The location of vortex roll-up shifts upstream from $x/D_{inj} \approx 5$ for $p_\infty = 6.9$ MPa to $x/D_{inj} \approx 3$ for $p_\infty = 9.3$ MPa. In addition, the jet spreads further and the length of the potential core decreases to $6–7D_{inj}$ in the latter case.

Abnormal variations of thermophysical properties are observed, as shown, for example, in the thermal-diffusivity field, which exhibits a steep variation across the jet boundary. It decreases rapidly and reaches

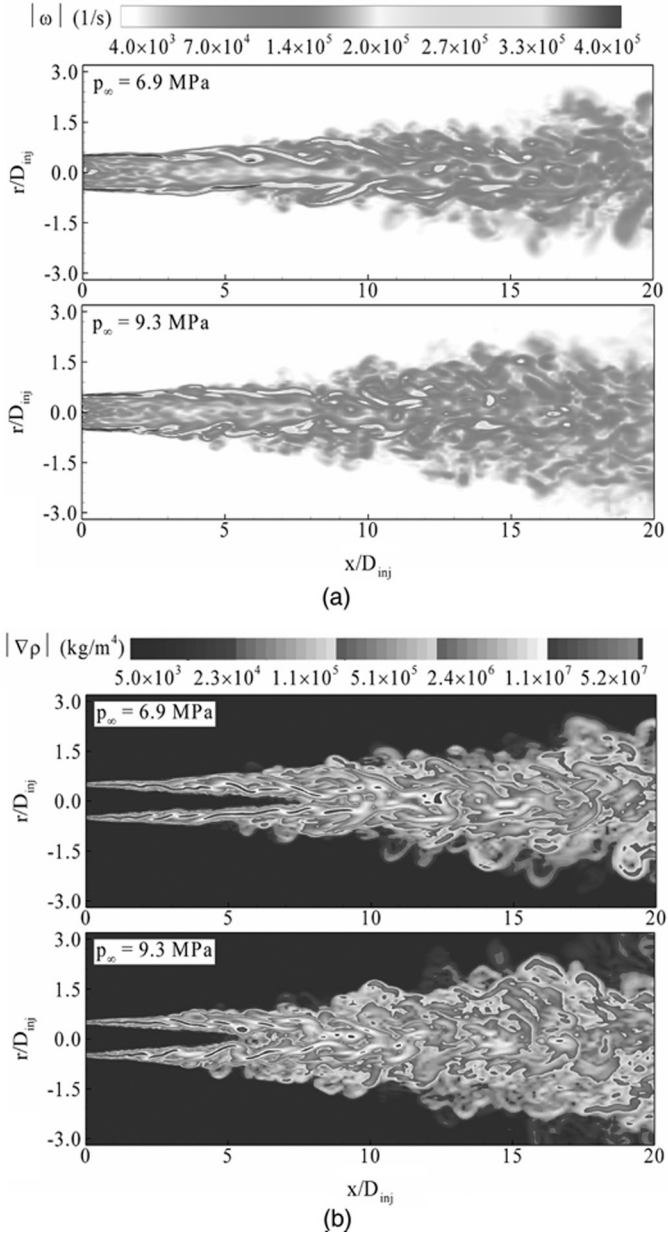

Figure 2. Effect of pressure on (a) vorticity-magnitude, (b) density-gradient magnitude, (c) thermal-diffusivity, and (d) compressibility-factor fields ($T_\infty = 300\,\mathrm{K}$, $u_{inj} = 15\,\mathrm{m/s}$, $T_{inj} = 120\,\mathrm{K}$, $D_{inj} = 254\,\mu\mathrm{m}$) (See Color Plate 11 at the end of this issue).

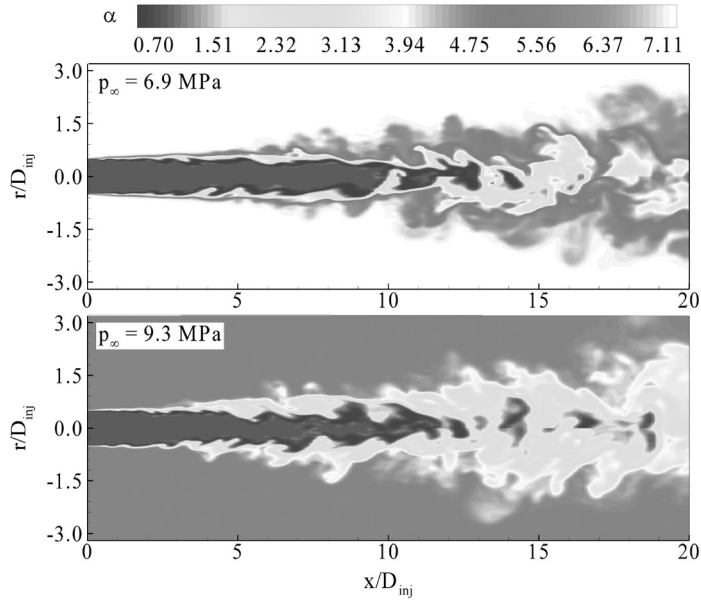

(c)

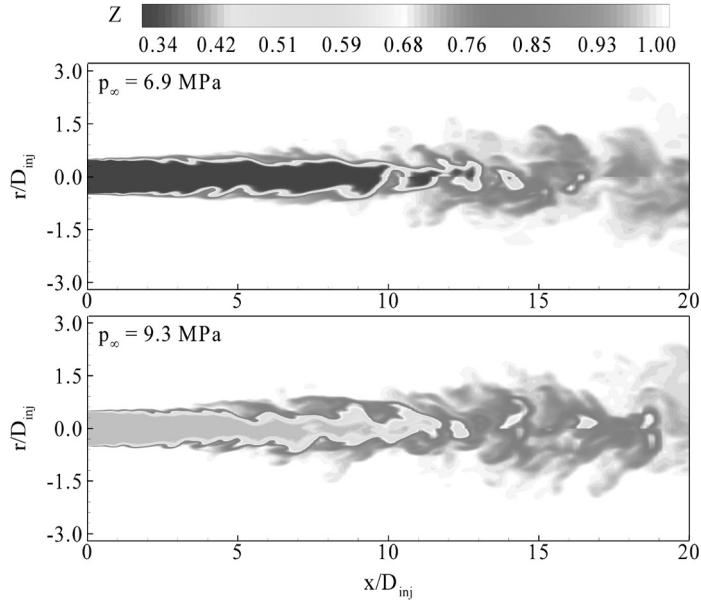

(d)

Figure 2. Continued.

Table 2. Most amplified frequency of initial shear layer instability at different pressures

	f (kHz)	$Sh = f\theta_0/\overline{u}$
6.9 MPa	34.8	0.048
9.3 MPa	37.2	0.051

a minimum as the fluid temperature transits through the inflection point on the isobaric curve (Zong et al., 2004). The compressibility factor, which measures the departure from ideal-gas behavior, has values of 0.34 and 0.42 in the jet core region for $p_\infty = 6.9$ MPa and 9.3 MPa, respectively. As the injected fluid mixes with the ambient gases, its temperature changes rapidly and its volume dilates. The compressibility-factor increases quickly and approaches unity at an axial location of $x/D_{inj} = 20$ on the centerline for $p_\infty = 6.9$ MPa, where the fluid behaves almost ideally.

The frequency spectra of pressure fluctuations at different axial locations along the shear layer ($r/D_{inj} = 0.5$) are acquired to quantitatively characterize the vortical dynamics and flow instability. The most amplified frequencies of the initial shear-layer instability at two different ambient pressures are presented in Table 2, where θ_0 and $\overline{u}$ are the momentum thickness and bulk velocity, respectively. The oscillations reach their respective maximum amplitudes at the axial locations of $x/D_{inj} = 3$ and 2, respectively. In the present study, $\theta_0 = 0.011$ mm and $\overline{u} = 8$ m/s, the most amplified frequencies fall into the Strouhal-number range of (0.044–0.048) for a planar mixing layer as suggested by Schadow and Gutmark (1992).

To provide more insight into the observed flow phenomena, a linear stability analysis was carried out on the effects of ambient pressure on the jet evolution (Liu et al., 2005). The work extends the approaches described by Yu and Monkewitz (1990) and Soteriou and Ghoniem (1995) to include real-fluid behavior. The SRK equation of state is implemented in the formulation. Each dependent variable is decomposed into a base and a perturbation quantity. The former is acquired directly from the numerical simulation of the flowfield. The latter takes the following general form for an axisymmetrical configuration

$$\widehat{\phi}(x, y, t) = \phi(y) \exp\{i(kx - \omega t)\} \tag{1}$$

where k and ω are the wave number and frequency, respectively. For a spatial instability problem, k is a complex variable and its negative

imaginary part represents the spatial growth rate. After substitution of the decomposed variables into the conservation laws and linearization of the result, a dispersion equation characterizing the relationship between the wave number and frequency can be derived in terms of pressure fluctuation as follows.

$$\frac{d^2\hat{p}}{dy^2} - \left(\frac{1}{\overline{\rho}} \cdot \frac{d\overline{\rho}}{dy} + \frac{2}{\overline{u} - \omega/k}\frac{d\overline{u}}{dy} - \frac{1}{y}\right)\frac{d\hat{p}}{dy} - k^2\hat{p} = 0 \tag{2}$$

The problem then becomes solving Eq. (2) for the eigenvalues k and ω subject to appropriate boundary conditions. A complete discussion of the stability analysis is given by Liu et al. (2005).

Figure 3 shows the spatial growth rates of the instability waves as a function of the normalized frequency (i.e., the Strouhal number) for three different pressures. The growth rate of the shear wave decreases with increasing pressure. The result confirms that the strong density stratification in the lower-pressure case suppresses the growth of disturbances and stabilizes the mixing layer. The linear stability analysis, in general, slightly underestimates the frequencies of the most unstable oscillations, compared with the numerical-simulation results.

The disintegration of the injected fluid jet is observed in the snapshot of iso-surfaces of different densities in Figure 4. The outer boundary of the jet is characterized by the density level of 80 kg/m^3, which is close to the ambient value of 77 kg/m^3, and the dense fluid core is delineated by the density level of 580 kg/m^3. The jet surface as delineated by the

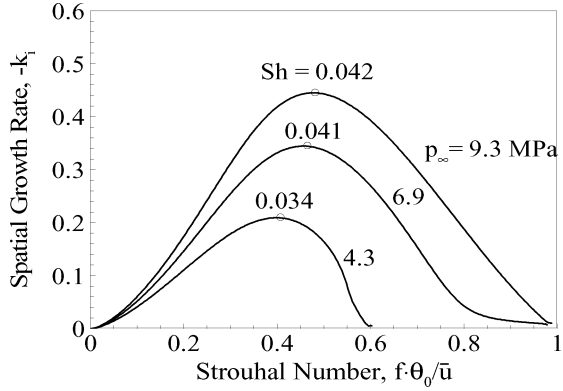

Figure 3. Spatial growth rate as function of Strouhal number for different pressures.

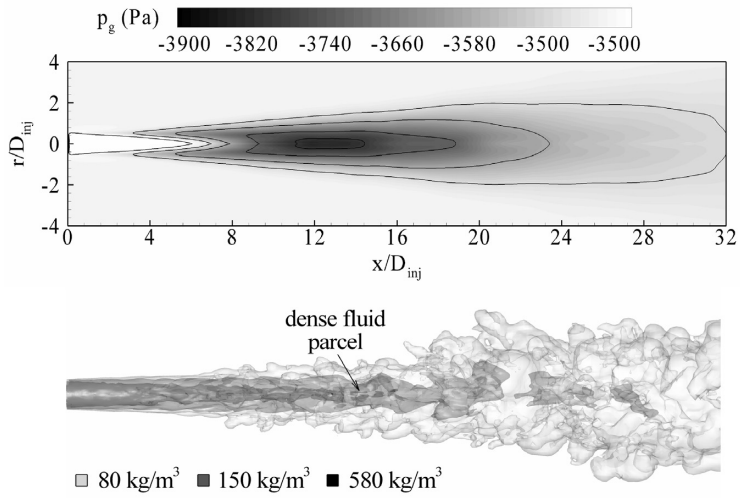

Figure 4. Mean pressure field and snapshot of density field showing dense fluid jet disintegration process, Case 1: $p_\infty = 6.9\,\text{MPa}$, $T_\infty = 300\,\text{K}$, $u_{inj} = 15\,\text{m/s}$, $T_{inj} = 120\,\text{K}$, $D_{inj} = 254\,\mu\text{m}$.

density level of $80\,\text{kg/m}^3$ is relatively smooth immediately downstream of the injector, but is then twisted by vortical waves and becomes irregular in all three spatial directions. As the injected fluid is convected downstream, the jet core becomes less cohesive. A series of dense fluid parcels is shed from the core region after the large-scale vortices pinch the centerline. Since the effect of interfacial thermodynamics disappears under supercritical conditions, the dense-fluid parcels dissolve into the environment in a diffusion/convection controlled mode, due to intensive turbulent mixing and rapid heat transfer from the surroundings. The frequency spectra of density variations at three different centerline locations downstream of the potential core (i.e. $x/D_{inj} = 10, 12,$ and 14) indicate a disintegration frequency of approximately 14.5 kHz. This value is slightly lower than the jet preferred mode frequency of 17.4 kHz measured at $x/D_{inj} = 9$ and $r/D_{inj} = 0.5$. The discrepancy between the two frequencies mainly results from the difference in measurement locations.

Accompanied by intensive mixing and severe variations of fluid properties, strong volume dilatation occurs in the transition region $(9 \leq x/D_{inj} \leq 25)$ and in the shear layer surrounding the jet. Such fluid expansion gives rise to a slight decrease in pressure. Consequently, a

distribution of negative gauge pressure, defined as the deviation between the local static pressure and chamber pressure, appears in those regions, as shown in the top plot of Figure 4.

To further validate the analysis and to characterize supercritical fluid jet mixing, the mean-flow and turbulence properties are calculated and compared with experimental results for cryogenic fluid jets at supercritical conditions (Chehroudi et al., 2002a, 2002b) and incompressible, variable-density jets (Amielh et al., 1996). Figure 5 shows the radial distributions of the normalized mean density, $\rho^* = (\overline{\rho} - \overline{\rho}_\infty)/(\overline{\rho}_c - \overline{\rho}_\infty)$, at different axial locations. The radial coordinate is normalized by the full-width-half-maximum (FWHM, denoted by $r_{1/2}$) based on the density at the axial position of concern. Three distinct flow regimes are identified, as for incompressible turbulent jets. The potential core is manifested by the flat-hat distribution near the injector. The

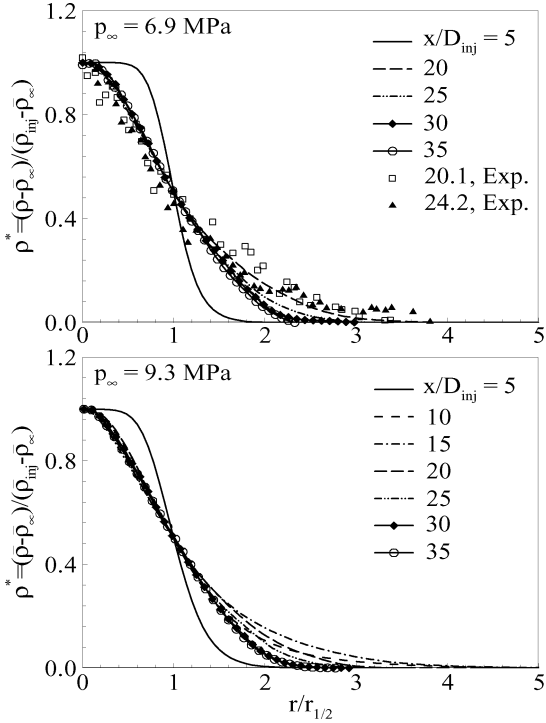

Figure 5. Radial distributions of normalized density at different axial locations ($T_\infty = 300\,\mathrm{K}$, $u_{inj} = 15\,\mathrm{m/s}$, $T_{inj} = 120\,\mathrm{K}$, $D_{inj} = 254\,\mu\mathrm{m}$).

density profiles merge into a single distribution farther downstream ($x/D_{inj} > 30$), suggesting the existence of a fully developed self-similarity region. A transition region occurs between 10 and $30D_{inj}$. The experimental data obtained using the Raman scattering technique for an ambient pressure of 6.9 MPa (Chehroudi et al., 2002a) is also plotted for comparison. Good agreement between calculations and measurements was achieved with a maximum deviation of 8%.

The spatial growth rate of a jet flow is usually assessed with a visual spreading angle (θ), determined by the outermost observable extent/boundary of the jet. On a shadowgraph image, θ can be measured as the angle between the centerline and the line originating from the edge of the injector exit and passing the outer boundary of the jet. An empirical correlation for the spreading angle of a cryogenic fluid jet under both sub- and super-critical pressures was proposed by Chehroudi et al. (2002b). The correlation is further combined with those for isothermal liquid sprays (Reitz and Bracco, 1979) and incompressible, variable-density turbulent jets (Papamoschou and Roshko, 1988) to have the following general form:

$$\theta = 0.27[F(\rho_\infty/\rho_{inj}) + (\rho_\infty/\rho_{inj})^{1/2}] \tag{3}$$

where

$$\begin{aligned} F(\rho_\infty/\rho_{inj}) &= 5.325\rho_\infty/\rho_{inj} + 0.0288 \quad && \rho_\infty/\rho_{inj} < 0.0885 \\ &= 0.5 && \rho_\infty/\rho_{inj} \geq 0.0885 \end{aligned} \tag{4}$$

Under the present flow conditions for cryogenic nitrogen jets, ρ_∞/ρ_{inj} is greater than 0.0885 and a constant of 0.5 is adopted for the function F. The jet boundary is defined as twice the density FWHM($r_{1/2}$), following the suggestion of Chehroudi et al. (2002b). Figure 6 shows good agreement of the calculated jet spreading angles with the prediction by Eq. (3). The maximum deviation is 5%. Both the simulation and experimental results match the correlation proposed by Dimotakis (1986) for incompressible, variable-density mixing layers.

Figure 7 shows the normalized turbulence intensities along the centerline. Compared with incompressible, variable-density jets (Amielh et al., 1996), the turbulent kinetic energy in a supercritical jet remains basically unchanged along its prolonged potential core, due to the reduced shear-layer instability caused by the stabilizing effect of density stratification. The turbulence intensity then increases rapidly, reaches a

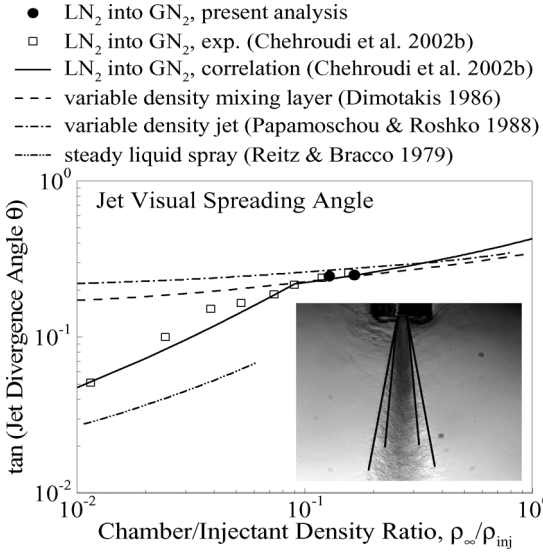

Figure 6. Tangent of jet visual spreading angle as function of chamber/injectant density ratio.

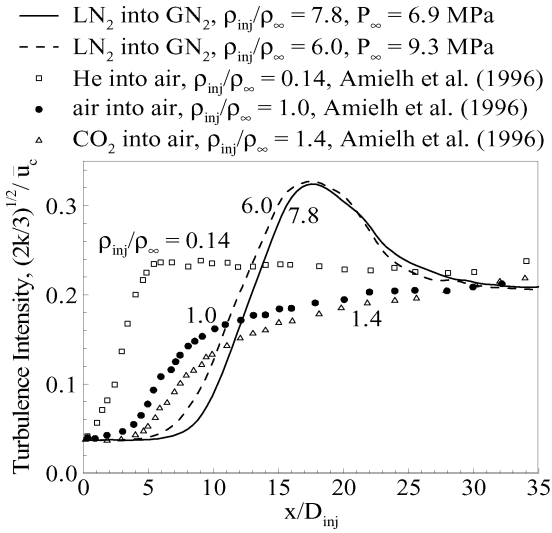

Figure 7. Distribution of normalized turbulence intensity along jet centerline ($T_\infty = 300$ K, $u_{inj} = 15$ m/s, $T_{inj} = 120$ K, $D_{inj} = 254$ μm).

maximum of 32% around the axial location of $x/D_{inj} = 18$, and then levels down to a value close to its counterpart in an incompressible jet. Such a severe variation in turbulence intensity is mainly attributed to the vigorous variations in fluid properties, as evidenced in Figure 2, and the ensuing mixing enhancement in the transition region, $10 \leq x/D_{inj} \leq 25$. A similar phenomenon was observed by Zhou et al. (2001) in their numerical simulations of turbulent buoyant jets, in which the overshoot of the turbulent kinetic energy was caused by the buoyance-induced secondary instability.

DYNAMICS OF SIMPLEX SWIRL INJECTOR

The dynamics of cryogenic oxygen injected through a simplex swirl injector operating at supercritical pressure is investigated in this section. This type of injector has been employed widely in contemporary liquid-propellant rocket engines, because of their improved intra-element mixing efficiency as compared with shear coaxial injectors (Bazarov et al., 2004). The injector consists of three major parts: tangential inlets, a vortex chamber, and a discharge nozzle, as shown schematically in Figure 8. The important geometrical parameters employed in the present study are listed in Table 3 (Zong and Yang, 2004), where R_s, R_n, and R_p denote the radii of the vortex chamber, discharge nozzle, and tangential

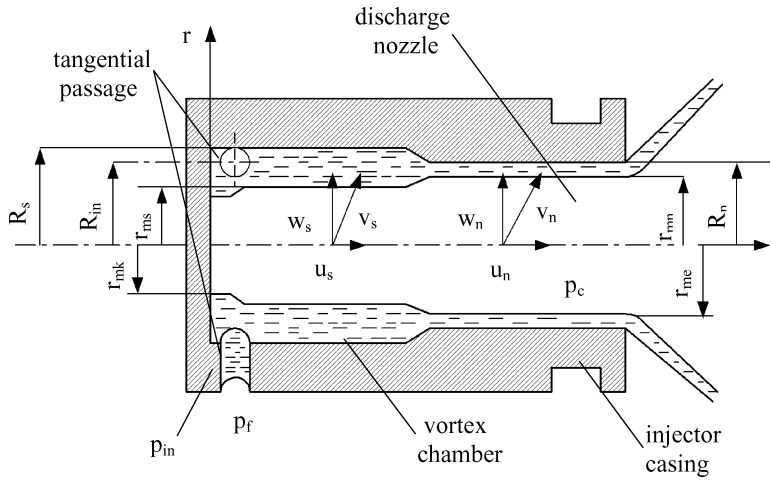

Figure 8. Schematic of simplex swirl injector.

Table 3. Geometric parameters and mass flow rate of simplex swirl injector

R_s (mm)	R_n (mm)	R_p (mm)	L (mm)	K	$\dot{m}$ (kg/s)
2.5	2.5	0.85	25	3.2	0.15

inlet, respectively, and L the overall injector length. The injector geometry and mass flow rate are chosen to be identical to those of the central LOX post of the swirl coaxial injector in the RD-0110 liquid rocket engine (Rubinsky, 1996). The geometrical characteristic constant K, which determines the swirling strength of the injected fluid, is defined as $K \equiv A_n R_{in}/A_{in} R_n$, with A_n being the nozzle area, A_{in} the total area of the tangential inlets, and R_{in} the radial location of the tangential entry.

Two representative scaling parameters, the liquid film thickness h at the injector exit and the spray cone angle α, are often employed to describe LOX swirling jets (Bazarov et al., 2004). The former dictates the size of the fluid parcel after the film breaks up, and the latter affects the intra-element mixing efficiency of a swirl coaxial injector. The spray cone angle is defined as twice the apex angle of the asymptotic cone to the hyperboloid of revolution corresponding to the profile of the spray (Tanasawa and Kobayasi, 1955), which is measured as the ratio of the circumferential to the axial velocities at the injector exit (i.e., $\tan \alpha/2 \equiv w_n/u_n$). Other physical variables needed to describe the flow evolution under supercritical conditions include the injector geometric constant K, injector length L, injector exit diameter D_n, and thermophysical properties of the fluids. According to the Buckingham Pi theorem, two dimensionless equations can be obtained to correlate these variables (Zong and Yang, 2004):

$$h/D_n = g(\rho_{inj}/\rho_\infty, \mu_{inj}/\mu_\infty, \mathrm{Re}_L, K) \tag{5}$$

$$\alpha/2 = \tan^{-1} u_n/w_n = g(\rho_{inj}/\rho_\infty, \mu_{inj}/\mu_\infty, \mathrm{Re}_L, K) \tag{6}$$

where ρ and μ are the density and viscosity of the fluid, respectively. The Reynolds number is defined as $\mathrm{Re}_L = \rho_{inj} u_n L/\mu_{inj}$. The density and viscosity ratios are determined by the operating conditions, and the remaining parameters depend on the injector geometry.

The internal flow dynamics of a liquid swirl injector at low and moderate pressures have been extensively studied (Bazarov et al., 2004). Application of the conservation laws of energy and angular momentum

for an invisid flow, along with the maximum flow principle (Abramovich, 1976), shows that the liquid film thickness and spray cone angle are functions only of the injector geometric constant K

$$K = (1 - \varphi)\sqrt{2}/\varphi\sqrt{\varphi} \tag{7}$$

$$\alpha/2 = \tan^{-1}\sqrt{2(1-\varphi)^2/[2 - \varphi - 2(1-\varphi)^2]} \tag{8}$$

where the coefficient of passage fullness, φ, can be related to the liquid film thickness h as

$$\varphi = 1 - (R_n - h)^2/R_n^2 \tag{9}$$

It is noteworthy that viscous losses inside the injector are neglected in this classical theory for incompressible flows.

A parametric study was conducted to investigate the influence of injector geometry and flow conditions on the injector dynamics. The test conditions are detailed in Table 4, where ΔL is the distance between the tangential entry and the injector head end. The pressure and temperature of the ambient gaseous oxygen are fixed at 100 atm and 300 K, respectively. The injected oxygen temperature is 120 K. For reference, the critical pressure and temperature of oxygen is 50.4 atm and 154.6 K, respectively. Also included in Table 4 are the calculated liquid film thickness and spray cone angle, for comparison with the predictions from classical theories for inviscid, incompressible flows (denoted by the subscript *inv*).

Table 4. Effect of injector geometry and flow conditions on LOX fluid film thickness and spray cone angle*

Cases	L (mm)	ΔL (mm)	K	$\dot{m}$ (kg/s)	Re_L	h (mm)	$\tan\frac{\alpha}{2}$	h_{inv}(mm)	$\tan\frac{\alpha_{inv}}{2}$
1	25	2.0	3.2	0.15	5.4×10^6	0.686	0.752	0.56	1.04
2	25	2.0	3.2	0.10	3.8×10^6	0.660	0.749	0.56	1.04
3	25	2.0	3.2	0.20	7.6×10^6	0.632	0.744	0.56	1.04
4	25	0.5	3.2	0.15	5.7×10^6	0.660	0.781	0.56	1.04
5	25	4.5	3.2	0.15	4.9×10^6	0.672	0.760	0.56	1.04
6	25	2.0	3.2	0.15	1.1×10^7	0.709	0.747	0.56	1.04
7	75	2.0	3.2	0.15	1.6×10^7	0.738	0.727	0.56	1.04
8	100	2.0	3.2	0.15	2.2×10^7	0.796	0.698	0.56	1.04
9	25	2.0	4.2	0.15	5.8×10^6	0.595	0.950	0.50	1.27

*$p_\infty = 10$ MPa and $\rho_{inj}/\rho_\infty = 7.6$.

The computational domain includes the swirl injector and a downstream region, as described by Zong and Yang (2004). A cylindrical sector with period boundaries specified in the azimuthal direction is considered, so that the main flow characteristics can be captured in a numerically efficient manner. The tangential inlet is simplified as a 1 mm wide slit on the radial wall of the injector, where the azimuthal and radial velocities are calculated based on the geometric constant K and mass flowrate $\dot{m}$. A typical simulation employs a 50×100 grid for the injector interior, and a 150×200 grid for the downstream-extension region. The grids are clustered near the wall and close to the injector exit to resolve the boundary layer and rapid flow property variations.

Figure 9 presents the mean temperature and velocity fields for Case 1. Cryogenic oxygen is introduced tangentially into the injector. The radial pressure gradient originating from the centrifugal force prevents the injected fluid from penetrating into the central region. Consequently, the momentum flux transfers from the radial to the axial direction, and the injected fluid convects downstream as a thin film along the injector wall. A whirling gas core, known as the cavity, forms in the central

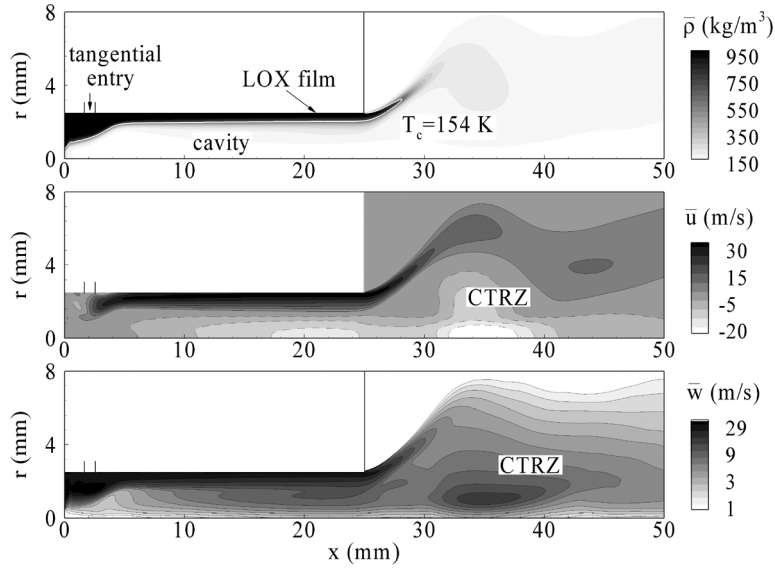

Figure 9. Mean density and axial and tangential velocity fields in simplex swirl injector ($p_\infty = 10$ MPa, $T_{inj} = 120$ K, $T_\infty = 300$ K, $\dot{m} = 0.15$ kg/s, $K = 3.2$, $\Delta L = 2.0$ mm).

region. The bright white contour in the density field corresponds to the critical isotherm ($T_c = 154.6$ K), which roughly represents the injected fluid boundary. As the LOX film discharges into the downstream chamber, it spreads outward and mixes with the ambient gaseous oxygen. The swirling strength also decreases during this process. Close to the injector exit, a slowly swirling gaseous region is observed, in which the adverse pressure gradient in the axial direction produces a central toroidal recirculation zone (CTRZ). Because the chamber pressure is well over the critical pressure of oxygen, there is no distinction between the injected fluid and the gas core. The boundary of the LOX film in the injector can be most conveniently characterized as the radial position above which the mass flow rate equals the specified value at the inlet. This definition takes full account of the variable-density effect. The film spreading angle can then be calculated, based on its definition, as the ratio of the averaged axial to azimuthal velocity component at the injector exit (Tanasawa and Kobayasi, 1955).

The effect of LOX mass flowrate on the injector dynamics was studied through Cases 1 to 3. In classical inviscid theory (Bazarov et al., 2004), both the film thickness and spray cone are independent of the mass flow rate, and depend only on the geometric constant K, as shown in Eqs. (7) and (8). In practice, the film thickness decreases slightly with increasing mass flow rate. The neglect of density variation and viscous losses in the theory leads to an underpredicted value. The spray cone angle is less susceptible to the LOX mass flow rate, although the theory overpredicts the quantity by almost 25%.

Figure 10 presents snapshots of the temperature fields with different mass flowrates. A thin LOX film along the wall and a gas core in the center region are clearly observed in the injector. As the LOX film is discharged into the chamber, a sinuous line of Kelvin–Helmholtz billows appear and grow up into ring vortices. The vortex shedding frequency is around 1160 Hz for Case 2. As the mass flowrate increases, the film penetrates more deeply into the chamber and leads to an elongated center recirculation zone. The associated vortex shedding frequencies, however, decrease to 960 Hz and 830 Hz for Cases 1 and 3, respectively.

The influence of the tangential inlet position on the injector performance was explored through Cases 2, 4, and 5. The film thickness increases as the tangential entry is moved away from the injector head end. This contradicts classical boundary theory, which suggests that the thickness of the liquid film increases as the distance from

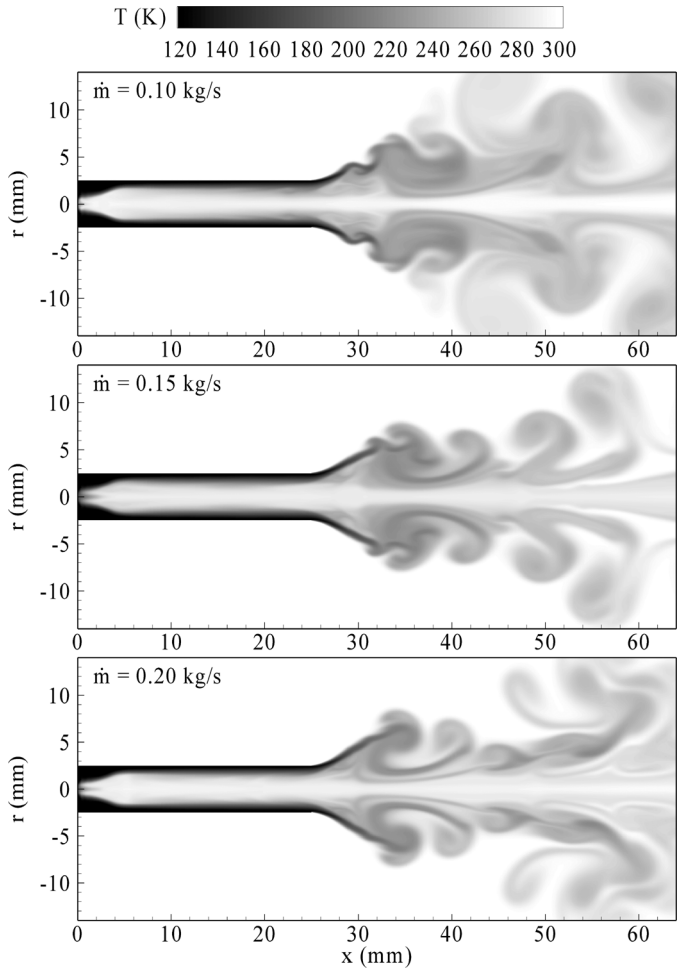

Figure 10. Effect of mass flow rate on temperature field ($p_\infty = 10\,\text{MPa}$, $T_{inj} = 120\,\text{K}$, $T_\infty = 300\,\text{K}$, $K = 3.2$, $\Delta L = 2.0\,\text{mm}$).

the inlet increases. To explore this phenomenon, the instantaneous streamlines near the head end are examined in Figure 11. When the tangential inlet is located downstream (i.e., Case 5), part of the injected fluid moves upstream and forms a recirculation region, producing an extra momentum loss and consequently decreasing the flow velocity. The maximum spray cone angle occurs when the inlet is attached to the head end.

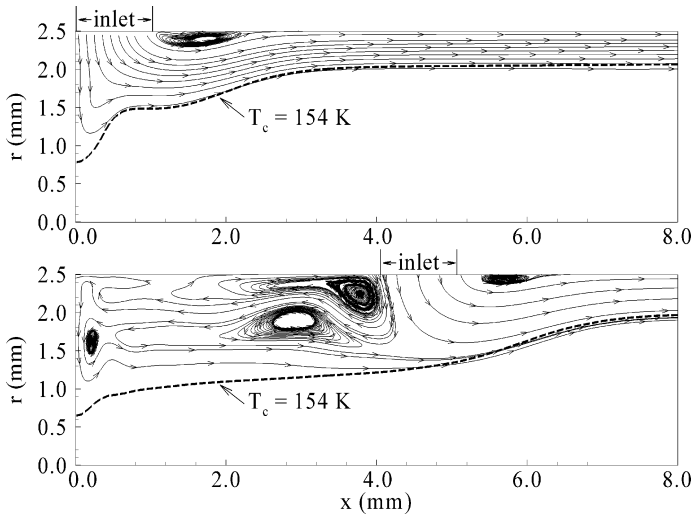

Figure 11. Effect of tangential entry position on flow evolution near the head end ($p_\infty = 10\,\text{MPa}$, $T_{inj} = 120\,\text{K}$, $T_\infty = 300\,\text{K}$, $\dot{m} = 0.15\,\text{kg/s}$, $K = 3.2$).

Owing to the layout of the propellant feed system, the length-to-diameter ratio of a liquid-rocket swirl injector is much greater than that of its counterpart for air-breathing engines (Bazarov et al., 2004). Therefore, the viscous loss along the wall exerts a strong influence on the injection process and hence alters the spray distribution and atomization efficiency. The simulation results for Cases 1 and 6–8 indicate that an increased injector length impairs two aspects of the performance: (1) increased liquid film thickness and resultant droplet size; and (2) reduced spreading angle of the liquid sheet.

The effects of swirling strength were examined in Cases 1 and 9. A swirl injector with a larger geometric constant K in general results in a greater azimuthal velocity and stronger swirling motion, which eventually gives rise to a thinner liquid film with a wider spreading angle. As a consequence, a better injector performance can be achieved by increasing K.

SHEAR COAXIAL INJECTION AND MIXING OF OXYGEN AND METHANE

For future development of high-performance reusable liquid rocket engines, mixing and combustion of LOX and hydrocarbon fuels has

recently attracted considerable interest. In this section, the flow dynamics of a shear coaxial injector using LOX and methane as propellants under supercritical pressures are investigated. Figure 12 shows the model injector considered. Co-flowing methane (outer) and oxygen (inner) streams are injected through the inlet and separated by a central post, having a thickness of 0.3 mm. The inner diameters of the LOX post and the methane annulus are 1.2 and 2.4 mm, respectively. Fully developed turbulent pipe flows are assumed at the injector exit.

The computational domain downstream of the injector measures a length of 40δ and a radius of 12δ, where δ is the thickness of the LOX post. Such dimensions are sufficient to minimize the effect of the far-field boundary conditions on the near-field flow evolution. A quasi-axisymmetric simulation was conducted. The entire grid system consists of 360×200 points along the axial and radial directions, respectively. The mean grid size of 10 μm falls in the inertial subrange of the turbulent kinetic energy spectrum estimated based on the inlet Reynolds number of the oxygen stream. To resolve the wake region and the vortical structures which shed downstream from the rim of the LOX post, a total of 40 grid points are used to cover the LOX post in the radial direction.

The volume downstream of the injector is preconditioned with gaseous methane at 300 K and a reference pressure of 100 atm. The injection temperatures and velocities of the oxygen and methane streams

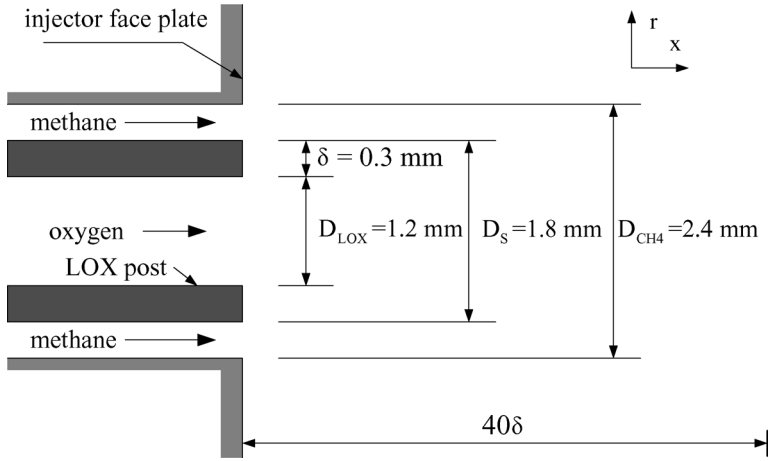

Figure 12. Schematic diagram of shear coaxial injector.

Table 5. Simulation conditions for analysis of supercritical LOX/methane injection and mixing process

	Case 1	Case 2
p (atm)	100	100
T_{LOX} (K)	150	150
T_{CH_4} (K)	150	220
T_∞ (K)	300	300
ρ_{LOX} (kg/m^3)	800	800
ρ_{CH_4} (kg/m^3)	360	180
ρ_∞ (kg/m^3)	75	75
u_{LOX} (m/s)	10	10
u_{CH_4} (m/s)	30	60
u_{CH_4}/u_{LOX}	3	6
$(\rho u)_{CH_4}/(\rho u)_{LOX}$	1.35	1.35
$(\rho u^2)_{CH_4}/(\rho u^2)_{LOX}$	4.05	8.1
$\dot{m}_{CH_4}/\dot{m}_{LOX}$	2.36	2.36
a_{LOX} (m/s)	461	461
a_{CH_4} (m/s)	1070	390
M_{LOX}	0.022	0.022
M_{CH_4}	0.028	0.154
Re_{LOX}	14.6×10^4	14.6×10^4
Re_{CH_4}	4.9×10^4	16.4×10^4

are varied to obtain a representative and comparable set of thermophysical and fluid dynamic characteristics. The relevant parameters are summarized in Table 5. The critical temperature and pressure of methane are 190 K and 46 atm, respectively. In Case 1, both fluids are at subcritical temperatures. In Case 2, the temperature of the methane stream is set at a supercritical value of $T_{CH_4} = 220$ K, and that of oxygen is fixed at $T_{LOX} = 150$ K. The injection velocities of the two streams are chosen to match the mass-flux ratio in the experiments conducted by Singla et al. (2004).

Figure 13 presents close-up views of the vorticity and oxygen mass-fraction fields near the injector. Three shear layers are observed: an inner layer emerging from the inner rim of the LOX post; and the other two from the inner and outer edges of the methane annulus. A series of large scale vortices shed from the outer rim of the LOX post. As those vortices grow, the two shear layers separated by the LOX post merge. Since the methane stream is faster in Case 2, the vortices formed downstream of

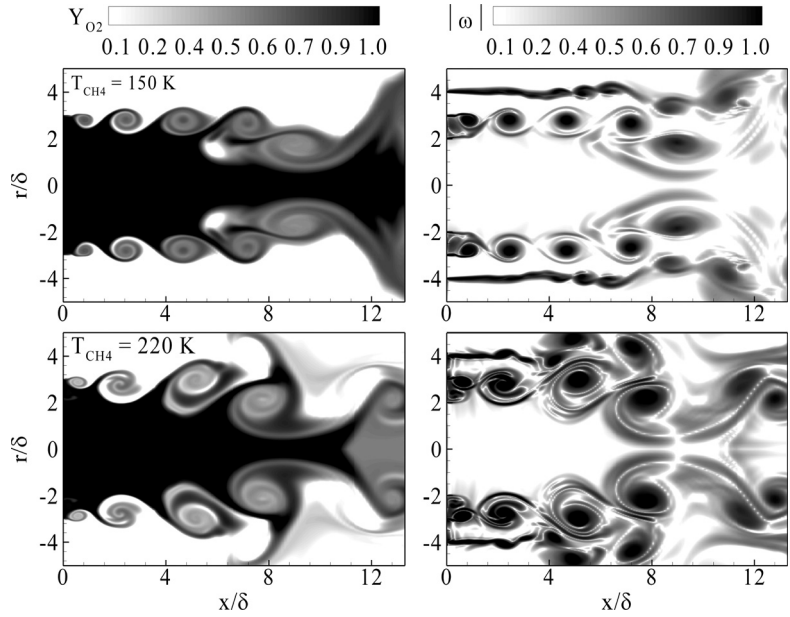

Figure 13. Snapshots of oxygen mass fraction and vorticity fields of shear coaxial injection of LOX and methane for Cases 1 and 2 in Table 5.

the LOX post are much stronger than those in Case 1. The mixing layer grows much faster and pinches the central line earlier, leading to an enhanced mixing between oxygen and methane.

Figure 14 shows snapshots of the methane mass-fraction, density, normalized vorticity, and velocity-vector fields immediately downstream of the LOX post. A string of large vortices shed from the outer rim of the LOX post in a manner analogous to that produced at a backward facing step. Although those energy-containing eddies concentrate on the lighter fluid side due to the density stratification, they entrain the denser oxygen much deeper into the methane stream and facilitate the mixing process. The density-stratification effect becomes more obvious in Case 2, where the eddies are apt to exist in the lighter fluid with the development of a large strain rate around the oxygen jet boundary. The wake behind the LOX post and the associated large-scale vortices can be further explored in the vorticity and velocity-vector fields. Those structures play a crucial role in determining the flame-stabilization characteristics of a shear co-axial injector (Oefelein and Yang, 1998).

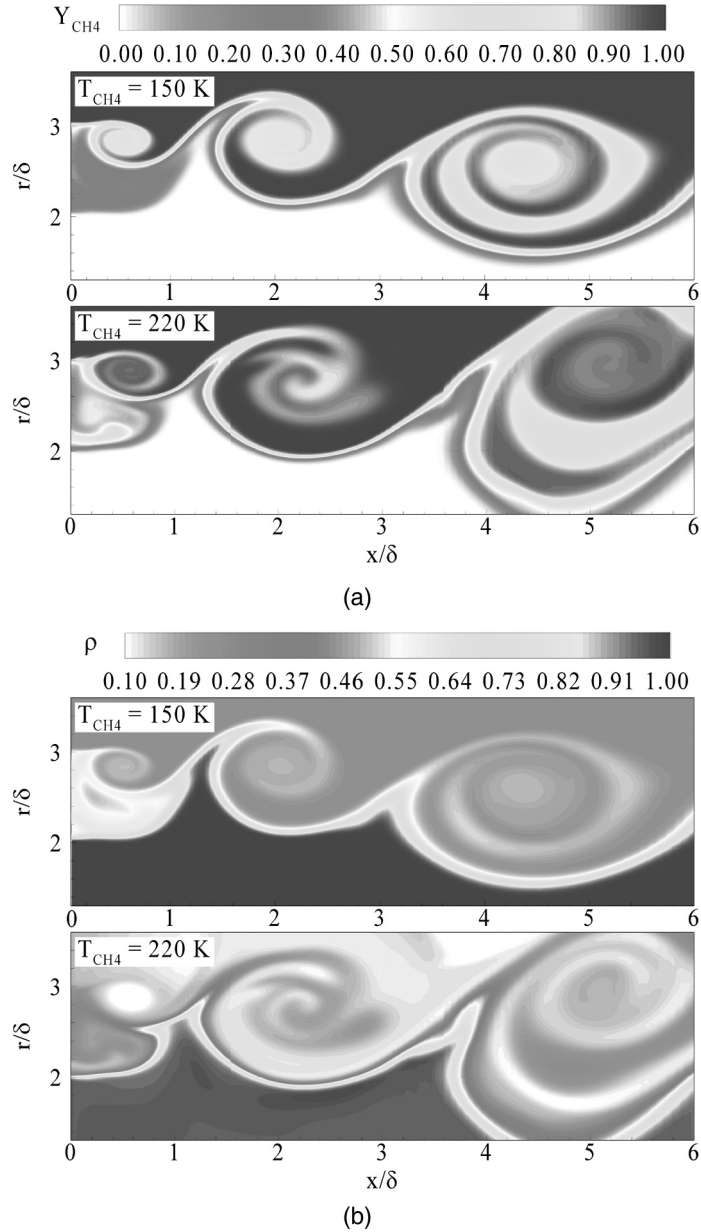

Figure 14. Close-up views of (a) methane mass fraction, (b) density, (c) vorticity, and (d) velocity-vector fields downstream of the LOX post for Cases 1 and 2 in Table 5 (See Color Plate 12 at the end of this issue).

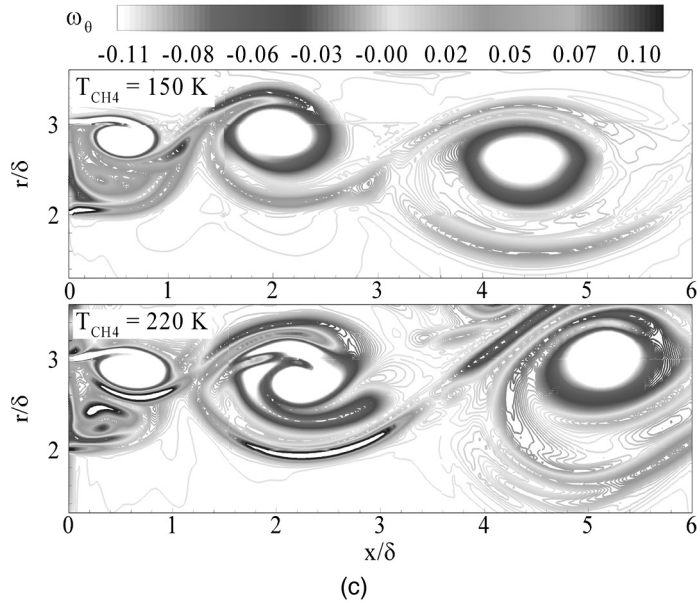

(c)

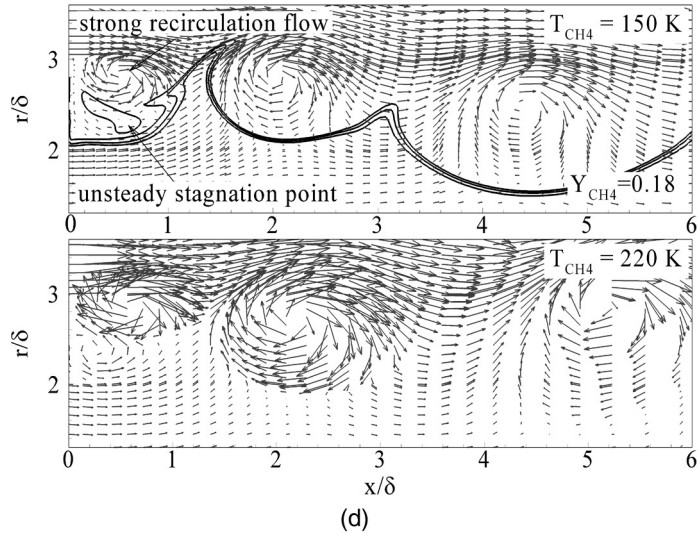

(d)

Figure 14. Continued.

The mixing of the LOX and methane streams results mainly from the dynamics of large eddies. Figure 15 shows the temporal evolution of the vorticity field over one cycle of vortex pairing. At the beginning, the vortices emerging from the LOX post are displaced to different radial locations due to their phase difference. These vortices then acquire different speeds, due to the nonuniformity of the flowfield. The vortex released at a later time may catch the earlier one, and merge into a single structure by kinematic induction. During this pairing process, the outer shear layer is engulfed deeply into the methane stream and breaks into a series of

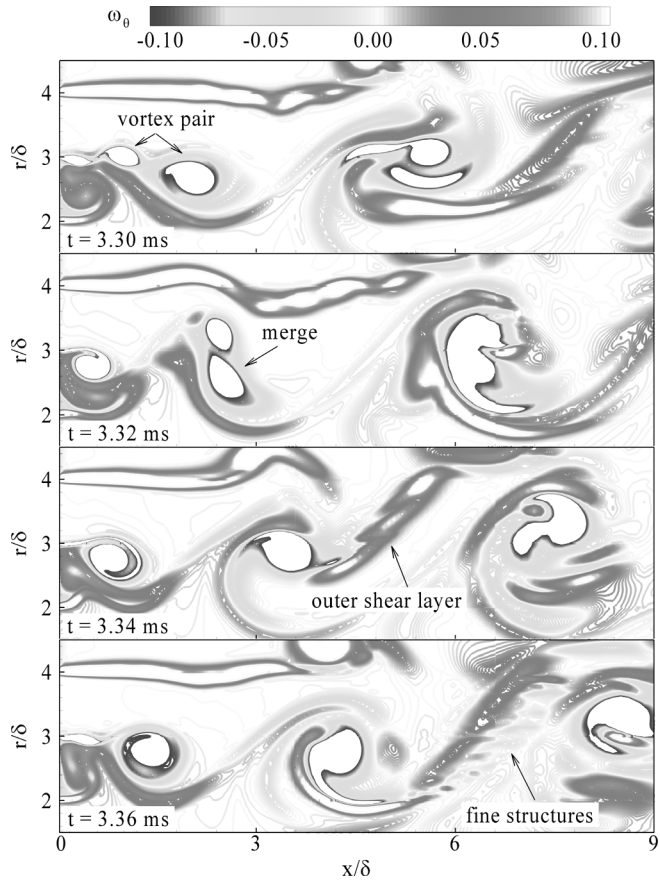

Figure 15. Temporal evolution of vorticity field over one cycle of vortex pairing of Case 1 in Table 5 (See Color Plate 13 at the end of this issue).

fine structures. The interfacial area grows during vortex pairing, providing more space for short-range molecular diffusion and enhancing the total yield of mixing.

The vortex-shedding frequencies behind the LOX post are obtained from the spectral contents of the pressure oscillations at different axial locations close to the injector. The results are 18.6 and 22.1 kHz for Cases 1 and 2, respectively. The dominance of the inner vortex string in the present study is in sharp contrast to the observations made by Rehab et al. (1997) and Carlos et al. (2003) for coaxial water jets without a splitter between two streams. They reported that the oscillations generated from the outer shear-layer were stronger. The existence of a second length scale (i.e., the LOX post thickness) in the present study significantly modifies the near-field flow dynamics. The vortices shed from the LOX post tip in a manner analogous to the vortex generated behind a backward facing step. The initial vortex-formation frequencies, normalized by the bulk velocity of the outer stream and the LOX post thickness, are on the order of $O(1)$ for both cases. The result is consistent with the theoretical analysis for a backward-facing step flow (Wee et al., 2004).

SUMMARY

A general theoretical and numerical framework, which accommodates full conservation laws and real fluid thermodynamic and transport phenomena, has been established. The model incorporates fundamental thermodynamics theories in such a manner that all the thermophysical properties can be determined directly. Turbulence closure is achieved using a large-eddy-simulation technique. The resultant analysis has been implemented to investigate a variety of supercritical fluid phenomena, including: 1) fluid jet dynamics, 2) swirl injection of liquid oxygen through a simplex swirl injector, and 3) shear co-axial injection and mixing of liquid oxygen and methane in transcritical and supercritical environments. Various intricacies associated with the evolution of fluid jets and mixing layers, including density stratification, shear-layer instability, volume dilatation, and property variations, are explored systematically. The flow dynamics are dictated largely by the local thermodynamic state through its influence on the fluid thermophysical properties. The importance of injector geometry and flow conditions on the swirl injector characteristics in terms of the resultant film thickness and spray spreading

angle, as well as the mixing efficiency, were identified. Results provide substantial insights into the behavior of cryogenic fluid flows over a broad range of thermodynamic states.

REFERENCES

Abramovich, G.N. (1976) Applied Gas Dynamics, Nauka, Moscow, Russia.

Amielh, M., Djeridane, T., Anselmet, F., and Fulachier, L. (1996) Velocity near field of variable density turbulent jets. *Int. J. Heat Mass Transfer*, **39**, 2149–2164.

Atsavapranee, P. and Gharib, M. (1997) Structures in stratified plane mixing layers and the effects of cross-shear. *J. Fluid Mech.*, **342**, 53–86.

Bazarov, V.G. and Yang, V. (1998) Liquid-propellant rocket engine injector dynamics. *J. Propul. Power*, **14**, 797–806.

Bazarov, V.G., Yang, V., and Puneesh, P. (2004) Design and dynamics of jet and swirl injectors. In Yang, V., Habiballah, M., Hulka, J., and Popp, M. (Eds.) *Liquid Rocket Thrust Chambers: Aspect of Modeling, Analysis, and Design*, Progress in Astronautics and Aeronautics, Vol. 200, pp. 19–104.

Branam, R. and Mayer, W. (2003) Characterization of cryogenic injection at supercritical pressure. *J. Propul. Power*, **19**, 342–355.

Candel, S., Juniper, M., Singla, G., Scouflaire, P., and Rolon, C. (2005) Structure and dynamics of cryogenic flames at supercritical pressure. To be published in *Combust. Sci. and Tech*.

Carlos, B., Guillaume, B., Patrick, B., and Olivier, M. (2003) Instability and transition in high velocity ratio coaxial jets: A Numerical Study. 3rd International Symposium on Turbulence and Shear Flow Phenomena, Sendai, Japan.

Chehroudi, B., Cohn, R., Talley, D., and Badakhshan, A. (2002a) Cryogenic shear layers: experiments and phenomenological modeling of the initial growth rate under subcritical and supercritical conditions. *Int. J. Heat Fluid Fl.*, **23**, 554–563.

Chehroudi, B. and Talley, D. (2002) Interaction of acoustic waves with a cryogenic nitrogen jet at sub- and super-critical pressures. AIAA Paper No. 2002-0342.

Chehroudi, B., Talley, D., and Coy, E. (2002b) Visual characteristics and initial growth rates of round cryogenic jets at subcritical and supercritical pressures. *Phys. Fluids*, **14**, 850–861.

Davis, D. and Chehroudi, B. (2004) The effects of pressure and acoustic field on a cryogenic coaxial jet. AIAA Paper No. 2004-1330.

Dimotakis, P.E. (1986) Two-dimensional shear-layer entrainment. *AIAA J.*, **21**, 1791–1796.

Ely, J.F. and Hanley, H.J. (1981) Prediction of transport properties. 1. Viscosity of fluids and mixtures. *Ind. Eng. Chem. Fundamentals*, **20**, 323–332.

Ely, J.F. and Hanley, H.J. (1983) Prediction of transport properties. 2. Thermal conductivity of pure fluids and mixtures. *Ind. Eng. Chem. Fundamentals*, **22**, 90–97.

Erlebacher, G., Hussaini, M.Y., Speziale, C.G., and Zang, T.A. (1992) Toward the large eddy simulation of compressible turbulent flows. *J. Fluid Mech.*, **238**, 155–185.

Graboski, M.S. and Daubert, T.E. (1978) A modified Soave equation of state for phase equilibrium calculation, 1. Hydrocarbon systems. *Ind. Eng. Chem. Proc. Design Dev.*, **17**, 443–448.

Habiballah, M., Orain, M., Grisch, F., Vingert, L., and Gicquel, P. (2005) Experimental studies of high pressure cryogenic flames on the Mascotte facility. To be published in *Combust. Sci. Tech*.

Hannoun, I.A., Fernando, H.J.S., and List, E.J. (1988) Turbulence structure near a sharp density interface. *J. Fluid Mech.*, **189**, 189–209.

Herding, G., Snyder, R., Rolon, C., and Candel, S. (1998) Investigation of cryogenic propellant flames using computerized tomography of emission images. *J. Propul. Power*, **14**, 146–151.

Ho, C.M. and Huerre, P. (1984) Perturbed free shear layers. *Ann. Rev. Fluid Mech.*, **16**, 365–422.

Hsieh, S.Y. and Yang, V. (1997) A preconditioned flux-differencing scheme for chemically reacting flows at all Mach numbers. *Int. J. Comput. Fluid Dyn.*, **8**, 31–49.

Hulka, J. and Makel, D. (1993) Liquid oxygen/hydrogen testing of a single swirl coaxial injector element in a windowed combustion chamber. AIAA Paper No. 1993-1954.

Hulka, J. and Schneider, J.A. (1991) Performance and stability of a booster class LOX/H2 swirl coaxial element injector. AIAA Paper No. 1991-1877.

Hulka, J. and Schneider, J.A. (1993) Single element injector cold flow testing for STME swirl coaxial injector element design. AIAA Paper No. 1993-2161.

Ivancic, B. and Mayer, W. (2002) Time- and length scales of combustion in liquid rocket thrust chambers. *J. Propul. Power*, **18**, 247–253.

Jacobsen, R.T. and Stewart, R.B. (1973) Thermodynamic properties of nitrogen including liquid and vapor phases from 63 K to 2000 K with pressure to 10,000 bar. *J. Phys. Chem. Ref. Data*, **2**, 757–922.

Juniper, M., Tripathi, A., Scouflaire, P., Rolon, C., and Candel, S. (2000) Structure of cryogenic flames at elevated pressures. *Proc. Combust. Inst.*, **28**, 1103–1109.

Kendrick, D., Herding, G., Scouflaire, P., Rolon, C., and Candel, S. (1999) Effects of recess on cryogenic flame stabilization. *Combust. Flame*, **118**, 327–339.

Liu, T., Zong, N., and Yang, V. (2005) Temporal and spatial stability of real-fluid mixing layer with density stratification. To be submitted to *Phys. Fluids*.

Mayer, W., Ivancic, B., Schik, A., and Hornung, U. (2001) Propellant atomization and ignition phenomena in liquid oxygen/gaseous hydrogen rocket combustors. *J. Propul. Power*, **15**, 794–799.

Mayer, W., Schik, A., Schaffler, M., and Tamura, H. (2000) Injection and mixing processes in high-pressure liquid oxygen/gaseous hydrogen rocket combustor. *J. Propul. Power*, **16**, 823–828.

Mayer, W. and Smith, J.J. (2004) Fundamentals of supercritical mixing and combustion of cryogenic propellants. In Yang, V., Habiballah, M., Hulka, J., and Popp, M. (Eds.) *Liquid Rocket Thrust Chambers: Aspect of Modeling, Analysis, and Design*, Progress in Astronautics and Aeronautics, Vol. 200, 339–368.

Mayer, W. and Tamura, H. (1996) Propellant injection in a liquid oxygen/gaseous hydrogen rocket engine. *J. Propul. Power*, **12**, 1137–1147.

Meng, H. and Yang, V. (2003) A unified treatment of general fluid thermodynamics and its application to a preconditioning scheme. *J. Comput. Phys.*, **189**, 277–304.

Meng, H., Hsiao, G.C., Yang, V., and Shuen, J.S. (2005) Transport and dynamics of liquid oxygen droplets in supercritical hydrogen streams. *J. Fluid Mech.*, **527**, 115–139.

Miller, R.S., Harstad, K.G., and Bellan, J. (2001) Direct numerical simulations of supercritical fluid mixing layers applied to heptane-nitrogen. *J. Fluid Mech.*, **436**, 1–39.

Oefelein, J.C. (2003) LES of supercritical LOX-H2 injection and combustion in shear-coaxial uni-element rocket. AIAA paper No. 2003-479.

Oefelein, J.C. (2005) Simulation and analysis of cryogenic LOX-H2 combustion processes at supercritical pressure. To be published in *Combust. Sci. Tech.*

Oefelein, J.C. and Yang, V. (1998) Modeling high-pressure mixing and combustion processes in liquid rocket engines. *J. Propul. Power*, **14**, 843–857.

Okong'o, N.A. and Bellan, J. (2002) Direct numerical simulation of a transitional supercritical binary mixing layer: heptane and nitrogen. *J. Fluid Mech.*, **464**, 1–34.

Okong'o, N.A. and Bellan, J. (2004) Turbulent and fluid-front area production in binary-species, supercritical, transitional mixing layers. *Phys. Fluids*, **16**, 1467–1492.

Okong'o, N.A., Harstad, K.G., and Bellan, J. (2002) Direct numerical simulation of O2/H2 temporal mixing layers under supercritical conditions. *AIAA J.*, **40**, 914–926.

Oschwald, M. and Schik, A. (1999) Supercritical nitrogen free jet investigated by spontaneous Raman scattering. *Exp. Fluids*, **27**, 497–506.

Oschwald, M., Smith, J.J., Branam, R., Hussong, J., Schik, A., Chehroudi, B., and Talley, D. (2005) Injection of fluid into supercritical environments. To be published in *Combust. Sci. Tech.*

Papamoschou, D. and Roshko, A. (1988) The compressible turbulent shear layer: An experimental study. *J. Fluid Mech.*, **197**, 453–477.

Rehab, H., Villermaux, E., and Hopfinger, E.J. (1997) Flow regimes of large-velocity-ratio coaxial jets. *J. Fluid Mech.*, **345**, 357–381.

Reitz, R.D. and Bracco, F.V. (1979) On the dependence of spray angle and other spray parameters on nozzle design and operating condition. SAE Paper no. 790494.

Rubinsky, V.R. (1996) Combustion instability in the RD-0110 Engine. In Yang, V. and Anderson, W. (Eds.) *Liquid Rocket Engine Combustion Instability*, Progress in Astronautics and Aeronautics, AIAA, Washington, DC, Vol. 169, pp. 89–112.

Sasaki, M., Sakamoto, H., Takahashi, M., Tomita, T., and Tamura, H. (1997) Comparative study of recessed and non-recessed swirl coaxial injectors. AIAA Paper No. 1997-2907.

Schadow, K.C. and Gutmark, E. (1992) Combustion instability related to vortex shedding in dump combustors and their passive control. *Prog. Energy Combust. Sci.*, **18**, 117–132.

Singla, G., Scouflaire, P., and Candel, S. (2004) Transcritical oxygen/transcritical or supercritical methane combustion. *Proc. Combust. Inst.*, **30**, 2921–2928.

Soteriou, M.C. and Ghoniem, A. (1995) Effects of the free-stream density ratio on free and forced spatially developing shear layers. *Phys. Fluids*, **7**, 2036–2051.

Strakey, P.A., Talley, D., and Hutt, J.J. (2001) Mixing characteristics of coaxial injectors at high gas/liquid momentum ratios. *J. Propul. Power*, **17**, 402–410.

Swanson, R.C. and Turkel, E. (1992) On central difference and upwind schemes. *J. Comput. Phys.*, **101**, 292–306.

Takahashi, S. (1974) Preparation of a generalized chart for diffusion coefficients of gases at high pressures. *J. Chem. Eng (Japan)*, **7**, 417–420.

Tanasawa, Y. and Kobayasi, K. (1955) A study on swirl atomizer. *Technical report of Tohoku University*, **20**, 27–58.

Wang, S.W., Hseih, S.Y., and Yang, V. (2005) Unsteady flow evolution in swirl injector with radial entry, Part I: Stationary conditions. *Phys. Fluids*, **17**, 045106.

Wee, D., Yi, T., Annaswamy, A., and Ghoniem, A.F. (2004) Self-sustained oscillations and vortex shedding in backward-facing step flows: Simulation and linear instability analysis. *Phys. Fluids*, **16**, 3361–3373.

Yang, V. (2000) Modeling of supercritical vaporization, mixing, and combustion processes in liquid-fueled propulsion systems. *Proc. Combust. Inst.*, **28**, 925–942.

Yu, M.H. and Monkewitz, P.A. (1990) The effect of nonuniform density on the absolute instability of two-dimensional inertial jets and wakes. *Phys. Fluids A*, **2**, 1175–1181.

Zhou, X., Luo, K.H., and Williams, J.J.R. (2001) Study of density effects in turbulent buoyant jets using large-eddy simulation. *Theoret. Comput. Fluid Dynamics*, **15**, 95–120.

Zong, N., Meng, H., Hsieh, S.Y., and Yang, V. (2004) A numerical study of cryogenic fluid injection and mixing under supercritical conditions. *Phys. Fluids*, **16**, 4248–4261.

Zong, N. and Yang, V. (2004) Dynamics of simplex swirl injectors for cryogenic propellants at supercritical conditions. AIAA Paper No. 2004-1332.

Zong, N. (2005) Modeling and simulation of cryogenic fluid injection and mixing dynamics under supercritical conditions. Ph.D. dissertation, Department of Mechanical and Nuclear Engineering, Pennsylvania State University, University Park, PA.

Zong, N. and Yang, V. (2005a) A numerical study of high-pressure oxygen/methane mixing and combustion of a shear coaxial injector. AIAA Paper No. 2005-0152.

Zong, N. and Yang, V. (2005b) An efficient preconditioning scheme for general fluid mixture using primitive variables. To be submitted to *J. Comput. Phys*.

Zurbach, S., Thomas, J.L., Verplancke, C., Vingert, L., and Habiballah, M. (2003) LOX/Methane studies for fuel rich preburner. AIAA Paper No. 2003-5063.